Article

Entropy Production Analysis in an Octagonal Cavity with an Inner Cold Cylinder: A Thermodynamic Aspect

Jiaul Haque Saboj [1], Preetom Nag [2] iD**, Goutam Saha [3,4]** iD **and Suvash C. Saha [4,]*** iD

[1] Department of Electrical and Computer Engineering, North South University, Dhaka 1229, Bangladesh
[2] Department of Mathematics and Physics, North South University, Dhaka 1229, Bangladesh
[3] Department of Mathematics, University of Dhaka, Dhaka 1000, Bangladesh; gsahamath@du.ac.bd
[4] School of Mechanical and Mechatronic Engineering, University of Technology Sydney, Ultimo, NSW 2007, Australia
[*] Correspondence: Suvash.Saha@uts.edu.au

Abstract: Understanding fluid dynamics and heat transfer is crucial for designing and improving various engineering systems. This study examines the heat transfer characteristics of a buoyancy-driven natural convection flow that is laminar and incompressible. The investigation also considers entropy generation (E_{gen}) within an octagonal cavity subject to a cold cylinder inside the cavity. The dimensionless version of the governing equations and their corresponding boundary conditions have been solved numerically using the finite element method, employing triangular mesh elements for discretization. The findings indicated that incorporating a cold cylinder inside the octagonal cavity resulted in a higher heat transfer (HT) rate than in the absence of a cold cylinder. Furthermore, using the heat flux condition led to a higher average Nusselt number (Nu_{avg}) and a lower Bejan number (Be) than the isothermal boundary condition. The results also showed that HT and E_{gen} were more significant in the Al_2O_3-H_2O nanofluid than the basic fluids such as air and water, and HT increased as χ increased. The current research demonstrates that employing the heat flux condition and incorporating nanoparticles can enhance the rate of HT and $Egen$. Furthermore, the thermo-fluid system should be operated at low Ra to achieve greater HT effectiveness for nanofluid concerns.

Keywords: octagonal cavity; natural convection; cylinder; entropy; heat transfer; ecological coefficient performance

1. Introduction

Scientists have been studying natural convection in cavities more frequently in the last few decades, as there are many real-world scenarios of it. Some of these are the cooling of electronic devices, heat exchangers [1,2], room ventilation [1], building insulation [1,2], and solar collectors [1,3], to name a few. To optimize the performance of these applications, it is crucial to understand the heat transfer mechanisms inside the cavity, which are influenced by several factors, such as the cavity's geometry, fluid properties, and boundary conditions. Understanding these parameters is essential for designing and carrying out efficient heat transfer systems in natural convection.

Alsabery et al. [1] performed a numerical investigation of entropy generation (E_{gen}) in a square cavity containing a nanofluid and a solid object. They studied how E_{gen} and heat transfer (HT) are affected by different temperature distributions. They observed that optimizing temperature distributions in natural convection systems can significantly improve their performance and efficiency. Sheremet et al. [3] employed a computational approach to examine the impacts of incorporating an isothermal partition made of solid material into a cavity filled with nanofluid, which was cooled by an isothermal cooler positioned at one of the corners. Their study unveiled that E_{gen} decreased as the parameter χ increased under increasing Ra conditions. Moreover, they discovered that utilizing nanofluids enhanced HT and lowered the Be value. Selimefendigil et al. [4] studied E_{gen}

in a nanofluid cavity with obstacles of different shapes. The researchers investigated the system while subject to the impact of a magnetic field and internal heat generation. Their investigation showcased that these techniques enhanced HT and resulted in a reduction of E_{gen} within the cavity. Their findings revealed that the shape of the obstacles significantly impacted HT and E_{gen}, and the use of nanofluids resulted in enhanced HT and reduced E_{gen}. Subsequently, Selimefendigil et al. [5] conducted a numerical examination of mixed convection and E_{gen} within a cavity filled with a power law fluid. The cavity featured a partial heater and a rotating cylinder, while a magnetic field also influenced the system. The research demonstrated that including a rotating cylinder led to augmented HT and diminished E_{gen} in the cavity. Furthermore, the study unveiled that implementing a magnetic field enhanced HT and reduced E_{gen} compared to scenarios where a magnetic field was not employed. Siavashi et al. [6] explored the realm of non-Darcy double-diffusive natural convection within inclined porous cavities, considering diverse source configurations. Their investigation unveiled that using inclined porous cavities with varying source arrangements enhanced HT and mitigated E_{gen}, in contrast to the absence of a source. Furthermore, the study emphasized the notable influence of the inclination angle on both HT and E_{gen}. Specifically, higher inclination angles yielded escalated heat transfer rates and reduced E_{gen}. Wang et al. [7] performed a computational study to analyze entropy generation in mixed convection within a square enclosure containing a rotating circular cylinder. Their study found results similar to Selimefendigil et al. [5], where a rotating cylinder increased HT and decreased E_{gen} in the cavity.

Rahimi et al. [8] analyzed E_{gen} and heatline visualization in a nanofluid-filled cavity with internal heaters. According to the research findings, the average Nusselt number (Nu_{avg}) increased when Ra and χ both increased. Furthermore, they observed a positive correlation between the total E_{gen} and Ra, indicating an increase in E_{gen} with higher Ra values. Conversely, the total E_{gen} n exhibited a negative relationship with χ, indicating a decrease in E_{gen} as χ values increased. In a subsequent study, Rahimi et al. [9] found results similar to that of Rahimi et al. [8]. The results of their study demonstrated that modifying the arrangement of rigid bodies within the refrigerant system is an effective strategy for managing the flow structure and temperature distribution. Kefayati et al. [10] performed a computational study to examine MHD natural convection and E_{gen} phenomena in a heated enclosure featuring two internally positioned cold cylinders filled with Carreau fluid. According to their findings, raising the buoyancy ratio increased E_{gen} and decreased Be_{avg}. They also discovered that an increase in Ha decreased the total E_{gen} and caused a considerable change in Be_{avg}. Arun et al. [11] investigated E_{gen} in a square cavity containing a rectangular block placed at the centerline position of the cavity. They observed that Ha, buoyancy ratio, and Ra influenced the flow patterns and rate of HT. Furthermore, their findings indicated that MHD and double-diffusive effects improved HT and decreased E_{gen} in the cavity. Bozorg et al. [12] numerically investigated the phenomenon of multi-phase mixed convection HT and E_{gen} within a cavity filled with a non-Newtonian fluid. The cavity had a rotating heater and cooler to facilitate the study. Their investigations indicated that the increase in Nu_{avg} that occurs with an increase in Ra becomes irrelevant when Ri is low. Moreover, they found that the heater and cooler cylinders' rotation significantly impacted the flow patterns and rate of HT.

Alsabery [13] studied mixed convection multi-phase flow in a cavity filled with nanofluid. The research findings showed that both Nu_{avg} and the convective HT increase when both Ra and the nanoparticle loading are increased. In a subsequent study, Alsabery [14] investigated the unsteady entropy generation in a flexible wall cavity containing a rotating cylinder. The findings indicated that the flexible wall impacted the flow, resulting in a rise in Nu_{avg} and a decrease in E_{gen}. These findings were consistent with those of Alsabery [13], which showed that using a rotating cylinder and nanofluid improved HT and reduced E_{gen} in the cavity. Ahrar [15] conducted a research study involving a numerical simulation of HT and E_{gen} in a cavity containing Al_2O_3-H_2O nanofluid. The impact of an external magnetic field source on the system was also investigated. According to the

study results, Nu_{avg} and the total E_{gen} of the system decreased as Ha increased. Tayebi and Chamkha [16] investigated E_{gen} analysis of MHD natural convection hybrid nanofluid flow in a cavity with a hollow cylinder. The study found that increasing buoyancy forces caused the rate of HT and E_{gen} due to HT, fluid flow, and magnetic effects, as well as the total E_{gen} to increase and Be_{avg} to decrease.

Tasmin et al. [17] studied the impact of non-Newtonian effects on HT and E_{gen} in natural convection flow inside a wavy nanofluid cavity. Their findings revealed that an increase in χ and Da leads to higher HT and lower E_{gen}. The undulating cavity was also discovered to impact the heat transfer phenomenon substantially. Li et al. [18] investigated MHD natural convection and E_{gen} characteristics of a nanofluid near a circular baffle positioned within an inclined square cavity, considering the influences of thermal radiation (Rd). Their findings indicated that Be decreased at low Ra values and increased at high Ra values when the baffle size was raised. They also found that increasing χ and Rd led to an increase in E_{gen}. Kashyap et al. [19] investigated E_{gen} in a square cavity for different Pr values containing hot blocks. Their study revealed that the rate of HT and E_{gen} increased with higher Ra and longer hot blocks. The research also showed that the flow behavior and E_{gen} are significantly impacted by Pr with a rise in the rate of HT and a decrease in E_{gen} observed with higher Pr. Hamzah et al. [20] examined E_{gen} within a vented cavity containing a heated cylinder situated between two counter-rotating cylinders. According to the study, increasing Ra and cylinder rotation increased the rate of HT and decreased E_{gen}.

Ahlawat et al. [21] explored the impacts of a heated block composed of a porous layer and nanofluid on convective HT and E_{gen} within a square cavity. The study findings indicated that the convective heat conduction from the heat source was enhanced as χ, Ra, and Da values increased. Majeed et al. [22] examined the thermal flows and E_{gen} within a hexagonal cavity through numerical simulation. Their research indicated that applying a magnetic field can boost the rate of HT and decrease the system's E_{gen}. Furthermore, their study suggests that magnetized hybrid nanomaterial could be served as effective heat transfer fluids. Acharya [23] conducted a study investigating the hydrothermal characteristics and entropy analysis of a buoyancy-driven MHD nanofluid flow within an octagonal cavity featuring fins. The study reveals that using fins enhanced HT and lower E_{gen} compared to a standard cavity case. Additionally, the research showed that raising Ra and χ led to an increase in the rate of HT and E_{gen}. Using a dynamic modulator, Ikram et al. [24] investigated the transient flow and HT analysis of forced convection in a partitioned, hexagonal air-filled cavity. Their findings showed that utilizing a dynamic modulator greatly enhanced heat transfer efficiency compared to a simple cavity configuration. Moreover, the study revealed that the rate of HT increased as Re increased. Considering a multi-blade modulator, Ikram et al. [25] further explored the unsteady characteristics of conjugate heat transfer in a hexagonal cavity. Their findings confirmed that using a multi-blade dynamic modulator enhanced the HT efficiency of the cavity. In 2023, Saha et al. [26] presented a configurative systematic review of the research on heat transfer in cavities. The systematic review covered a wide range of topics related to cavity heat transfer, including natural or mixed or forced convection, radiation, and magnetic field effects. This review indicated that using different boundary conditions, heat sources, and fluid types significantly affects HT performance in cavities.

In their study, Sharma et al. [27] demonstrated that an increase in the radiation parameter and volume fraction of nanoparticles contributes to an enhancement in the temperature profile. The study by Almuhtady et al. [28] encompassed an entropy analysis of a non-inclined cavity with a triangular fin filled with a variable porous media. They observed that the HT rate exhibited a decreasing trend with an increase in the inclination angle of the cavity. Ahmed and Rashad [29] investigated the impact of an irregular left boundary of a container filled with porous elements in the presence of a constant magnetic source. The study findings indicated that the undulation number and the wavy contraction ratio contribute to increased HT. Ahmed and Raizah [30] examined the non-Newtonian power law nanofluid flow between inclined polygonal/cylinder polygonal/polygonal forms,

employing the second law of thermodynamics. The key findings of the study revealed that the flow area and power-law index played significant roles in governing the convective and HT processes. Using a nanofluid, Raizah et al. [31] examined the flow and HT fields within a horizontal annulus partially saturated with a porous region. Their findings revealed that an increase in the solid volume fraction resulted in improved values of the Nu_{avg} while simultaneously reducing the average temperature and *Be*.

The author's knowledge and the available literature demonstrate the importance of investigating HT and E_{gen} in enclosed systems for multiple real-life scenarios, such as cooling systems and heat exchangers. The novelty of our study lies in the specific focus on HT and E_{gen} analysis in an octagonal cavity with an inner cold cylinder. While previous works have explored heat transfer phenomena in various cavity geometries, including rectangular and cylindrical configurations, the investigation of HT and E_{gen} in complex geometry, like an octagonal cavity with an inner cold cylinder, is relatively limited. This unique geometry introduces novel HT characteristics and potential applications in thermal management systems. This research aims to explore the impact of three distinct fluids—namely, air, water, and Al_2O_3-H_2O nanofluid—on HT features and the E_{gen} of an octagonal cavity housing a cold cylinder. This study aims to analyze the impact of various factors, including *Ra*, *Pr*, isothermal boundary condition (IBC), heat flux boundary condition (HFBC), and χ, on HT and E_{gen}. The outcomes will comprise assessments of Nu_{avg} and *Be*, as well as graphical representations of streamlines, isotherms, E_{gen} due to temperature gradients and fluid friction, local E_{gen}, and Bejan number (*Be*) contours to help comprehend HT traits and E_{gen} phenomena within the cavity.

2. Physical and Mathematical Model

Octagonal cavities possess substantial utility in diverse domains. The intricate geometry of an octagonal cavity renders it an apt object for investigating fluid flow and heat transfer. For instance, replacing the conventional rectangular or triangular shapes with octagonal cavities in heat exchangers can significantly elevate the rate and efficiency of heat transfer. Moreover, in electronic cooling systems, octagonal cavities promote heat transfer and minimize the likelihood of thermal damage to electronic components. Overall, due to its diverse engineering applications, the octagonal cavity represents a crucial research topic for analysis. This study can reveal valuable observations regarding the heat exchange characteristics of octagonal voids, thereby influencing the configuration and enhancement of enclosed thermal management systems in diverse engineering domains. This knowledge may lead to improved cooling efficiency, reduced energy consumption, and increased reliability in electronic devices. Details of the physical model are presented in Figure 1, and the properties of fluids and particles are shown in Table 1.

Table 1. Thermophysical properties at T = 293 K [32].

Physical Properties	H_2O	Al_2O_3
C_p [J/kgK]	4179	773
ρ [kg/m^3]	997.1	3880
k [W/mK]	0.613	36
$\beta \times 10^{-5}$ [1/K]	21	0.85

Figure 1 illustrates the octagonal cavity in which the octagon has a side length of L while the inner cylinder has a radius of 0.2 L. In the IBC case or HFBC case, the cylinder, along with the upper and lower horizontal walls, are regarded as cold (T_c), while the heated walls, located on the left and right sides, are maintained at a constant T_h (where $T_c < T_h$) in the IBC case or at a constant heat flux in the HFBC case. The remaining walls are adiabatic. The fluid flow being analyzed is assumed to be 2D, steady, incompressible, laminar, and Newtonian. The working fluids being studied are air, water, and Al_2O_3-H_2O nanofluid.

The volume concentrations of nanoparticles (χ) being considered range from 1% to 5%. Consequently, the Navier–Stokes equations governing fluid flow and energy are presented in a dimensionless format, as depicted below:

Continuity Equation:

$$\frac{\partial U}{\partial X} + \frac{\partial V}{\partial Y} = 0 \tag{1}$$

U-momentum equation:

$$\frac{\rho_{nf}}{\rho_f}\left[U\frac{\partial U}{\partial X} + V\frac{\partial U}{\partial Y}\right] = -\frac{\partial P}{\partial X} + \frac{\mu_{nf}}{\mu_f}Pr\left(\frac{\partial^2 U}{\partial X^2} + \frac{\partial^2 U}{\partial Y^2}\right) \tag{2}$$

V-momentum equation:

$$\frac{\rho_{nf}}{\rho_f}\left[U\frac{\partial V}{\partial X} + V\frac{\partial V}{\partial Y}\right] = -\frac{\partial P}{\partial Y} + \frac{\mu_{nf}}{\mu_f}Pr\left(\frac{\partial^2 V}{\partial X^2} + \frac{\partial^2 V}{\partial Y^2}\right) + Ra\,Pr\frac{(\rho\beta_T)_{nf}}{(\rho\beta_T)_f}\Theta \tag{3}$$

Energy Equation:

$$\frac{(\rho C_p)_{nf}}{(\rho C_p)_f}\left[U\frac{\partial \Theta}{\partial X} + V\frac{\partial \Theta}{\partial Y}\right] = \frac{\partial}{\partial x}\left(\frac{k_{nf}}{k_f}\frac{\partial \Theta}{\partial x}\right) + \frac{\partial}{\partial y}\left(\frac{k_{nf}}{k_f}\frac{\partial \Theta}{\partial y}\right) \tag{4}$$

where X and Y represent the non-dimensional Cartesian coordinates system, U and V represent the non-dimensional velocity components in the X and Y directions, Θ represents the non-dimensional temperature, and P represents the non-dimensional pressure. Subscripts f and nf indicate pure fluid and nanofluid, respectively. Here, $\rho_{nf} = \rho_f$, $\mu_{nf} = \mu_f$, $k_{nf} = k_f$, $Cp_{nf} = Cp_f$ and $(\rho\beta_T)_{nf} = (\rho\beta_T)_f$ for pure fluids such as air or water in the present study. The non-dimensional numbers that showed up in the governing equations are Ra and Pr.

$$\text{Isothermal boundary condition (IBC), } Ra = \frac{g\Delta T L^3\beta_f\rho_f}{\alpha_f\mu_f}$$

$$\text{Heat flux boundary condition (HFBC), } Ra = \frac{gL^4\beta_f\rho_f q''}{\alpha_f\mu_f k_f} \tag{5}$$

$$Pr = \frac{\nu_f}{\alpha_f}$$

To derive the non-dimensional Equations (1)–(4) from the associated dimensional equation, the following dimensionless parameters are utilized by Nag et al. [33]:

$$X = \tfrac{x}{L},\ Y = \tfrac{y}{L},\ U = \tfrac{uL}{\alpha_f},\ V = \tfrac{vL}{\alpha_f},\ P = \tfrac{pL^2}{\rho_f\alpha_f{}^2}$$

$$\Theta = \begin{cases} \frac{T-T_c}{\Delta T}, & \text{for IBC} \\ \frac{(T-T_{ref})k_f}{q''L}, & \text{for HFBC} \end{cases} \tag{6}$$

where, $\Delta T = T_h - T_c$ and T_{ref} is a reference temperature can be considered the cylindrical surface temperature. Furthermore, β_f, α_f, and g represent the coefficient of volumetric expansion, thermal diffusivity, and gravitational acceleration, respectively.

Boundary conditions

- For horizontal walls,

$$U = V = \Theta = 0 \tag{7}$$

- For vertical walls,

$$U = V = 0 \tag{8}$$

$$\text{For IBC}:\ \Theta = 1$$
$$\text{or for HFBC}:\ q'' = -1 \tag{9}$$

- For cylindrical surfaces,

$$U = V = \Theta = 0 \tag{10}$$

- For inclined walls,

$$U = V = \frac{\partial \Theta}{\partial \hat{n}} = 0 \tag{11}$$

where $\hat{n}$ denotes the outward normal vector.

Thermal properties of nanofluid

Determining the thermophysical properties of nanofluids is a complex task as there is uncertainty about which models can produce reliable results, and these models significantly impact the solutions. Researchers have proposed various thermophysical property models for nanofluids. However, due to their diversity and complexity, the thermophysical characteristics of nanofluids are still subject to debate, and no definitive conclusion has been reached for their use in flow and heat transfer applications. To calculate the thermophysical parameters of the nanofluid, the current investigation employs classical relationships between the base fluid and nanoparticles, as represented by the following equations.

The density of nanofluid is defined as Corcione [34]:

$$\rho_{nf} = (1 - \chi)\rho_f + \chi\rho_p \tag{12}$$

The heat capacitance of the nanofluid is defined as Corcione [34]:

$$(\rho C_p)_{nf} = (1 - \chi)(\rho C_p)_f + \chi(\rho C_p)_p \tag{13}$$

The thermal conductivity of the nanofluid is defined as Corcione [34]:

$$\frac{k_{nf}}{k_f} = 1 + 4.4 Re_p^{0.4} Pr_f^{0.66} \left(\frac{T}{T_{fr}}\right)^{10} \left(\frac{k_p}{k_f}\right)^{0.03} \chi^{0.66} \tag{14}$$

where Re_p is the nanoparticles Reynolds number, defined as

$$Re_p = \frac{\rho_f u_B d_p}{\mu_f} = \frac{2\rho_f k_b T}{\pi \mu_f^2 d_p} \tag{15}$$

The dynamic viscosity of the nanofluid is defined as Corcione [34]:

$$\frac{\mu_f}{\mu_{nf}} = 1 - 34.87 \left(\frac{d_p}{d_f}\right)^{-0.3} \chi^{1.03} \tag{16}$$

$$d_f = 0.1 \left(\frac{6M}{N\pi\rho_f}\right)^{\frac{1}{3}} \tag{17}$$

The thermal expansion coefficient of the nanofluid is defined as Corcione [34]

$$\frac{(\rho\beta_T)_{nf}}{(\rho\beta_T)_f} = (1 - \chi) + \chi\frac{(\rho\beta_T)_p}{(\rho\beta_T)_f} \tag{18}$$

Nusselt number

The average Nusselt number (Nu_{avg}) as Ahlawat et al. [21] and Saha et al. [35]:

- For isothermal conditions:

$$Nu_{avg} = \frac{k_{nf}}{k_f} \left[-\int_0^1 \frac{\partial\theta}{\partial x}\bigg|_{\text{left wall}} dy + \int_0^1 \frac{\partial\theta}{\partial x}\bigg|_{\text{right wall}} dy \right] \tag{19}$$

- For heat flux conditions:

$$Nu_{avg} = \frac{k_{nf}}{k_f}\left[-\int_0^1 \frac{1}{\theta}\bigg|_{\text{left wall}} dy + \int_0^1 \frac{1}{\theta}\bigg|_{\text{right wall}} dy \right] \tag{20}$$

Entropy generation

In order to evaluate the thermal efficacy of the system, the generation of entropy is analyzed. Therefore, this research was utilized as a criterion for evaluating the thermal performance within the cavity. In our investigation, thermal impacts and viscous impacts were responsible for E_{gen}. The local E_{gen}, $E_{l,t}$ is represented as follows in the non-dimensional form [36]:

$$E_{l,t} = S_{l,h} + S_{l,f}$$
$$S_{l,h} = \frac{k_{nf}}{k_f}\left[\left(\frac{\partial \theta}{\partial x}\right)^2 + \left(\frac{\partial \theta}{\partial y}\right)^2 \right] \tag{21}$$
$$S_{l,f} = \lambda \frac{\mu_{nf}}{\mu_f}\left[2\left(\frac{\partial u}{\partial x}\right)^2 + 2\left(\frac{\partial v}{\partial y}\right)^2 + \left(\frac{\partial u}{\partial y} + \frac{\partial v}{\partial x}\right)^2 \right]$$

where

$$\lambda = \frac{\mu_f T_0 \alpha_f^2}{k_f L^2 \Delta T^2} \tag{22}$$

Here, λ represents the irreversibility factor and is equal to 10^{-4}. It should be mentioned that when no particles are added, $k_{nf} = k_f$ and $\mu_{nf} = \mu_f$.

The local Bejan number (Be_l) [36]:

$$Be_l = \frac{S_{l,h}}{S_{l,h} + S_{l,f}} \tag{23}$$

The average entropy generation (E_{avg}):

$$E_{avg} = \frac{\int_0^1 \int_0^1 E_{l,t}\, dx\, dy}{\int_0^1 \int_0^1 dx\, dy} \tag{24}$$

The average Bejan number (Be) [36]:

$$Be = \frac{\int_0^1 \int_0^1 Be_l\, dx\, dy}{\int_0^1 \int_0^1 dx\, dy} \tag{25}$$
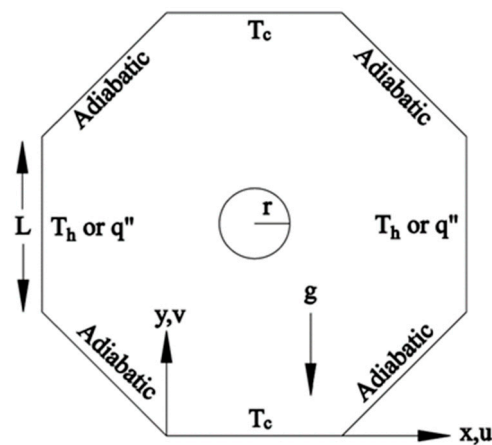

Figure 1. Illustration depicting the model's structure.

3. Numerical Modelling

The governing Equations (1)–(4) with corresponding boundary conditions, Equations (7)–(11), have been performed using the finite element method (FEM). The governing PDEs are trans-

formed into integral equations in this simulation methodology by applying the Galerkin weighted residual technique. The graphical results in our study are computed using the finite element method with a second-order approximation. It provides smooth solutions throughout the interior domain, even in the corner regions. This strategy will significantly improve fast convergence assurance. In this study, a non-uniform triangular mesh arrangement is implemented. The error criteria are evaluated with a relative tolerance of 10^{-6}.

4. Meshing and Validation

Grid Independent Test:

A grid-independent test was conducted on the simulation to ensure accuracy and reliability by running it with different grid sizes while keeping other parameters constant. The test aimed to determine the optimal grid size. In this study, the test was performed using a triangular mesh and eight grid sizes ranging from 11,960 to 57,116 elements, and the results are presented in Table 2. Based on the comparison, a grid size of 29,704 was selected for the simulations in this study.

Validation:

Figure 2 displays the streamlines and isotherms for incompressible flow at $Ra = 10^5$ and $Ra = 10^6$ in an octagonal cavity. The results obtained are qualitatively in good agreement with previous findings reported by Saha et al. [35]. Moreover, in Figure 3, a comparison is made between the current isotherm results and the numerical isotherm obtained through the CIP thermal LBM, as presented in the study conducted by Mussa et al. [37], as well as experimental results reported by Corvaro et al. [38]. The comparison was made for a rectangular cavity filled with air and heated by a small, localized heat source on the bottom wall. The figures demonstrate a clear agreement between the outcomes. To further validate the accuracy of the numerical simulation, the results for entropy generation are compared with those published in Ilis et al. [36] for square geometries. The excellent agreement between the present results for $S_{l,h}$, $S_{l,f}$, $E_{l,t}$, and Be_l and the previous studies is shown in Figure 4.
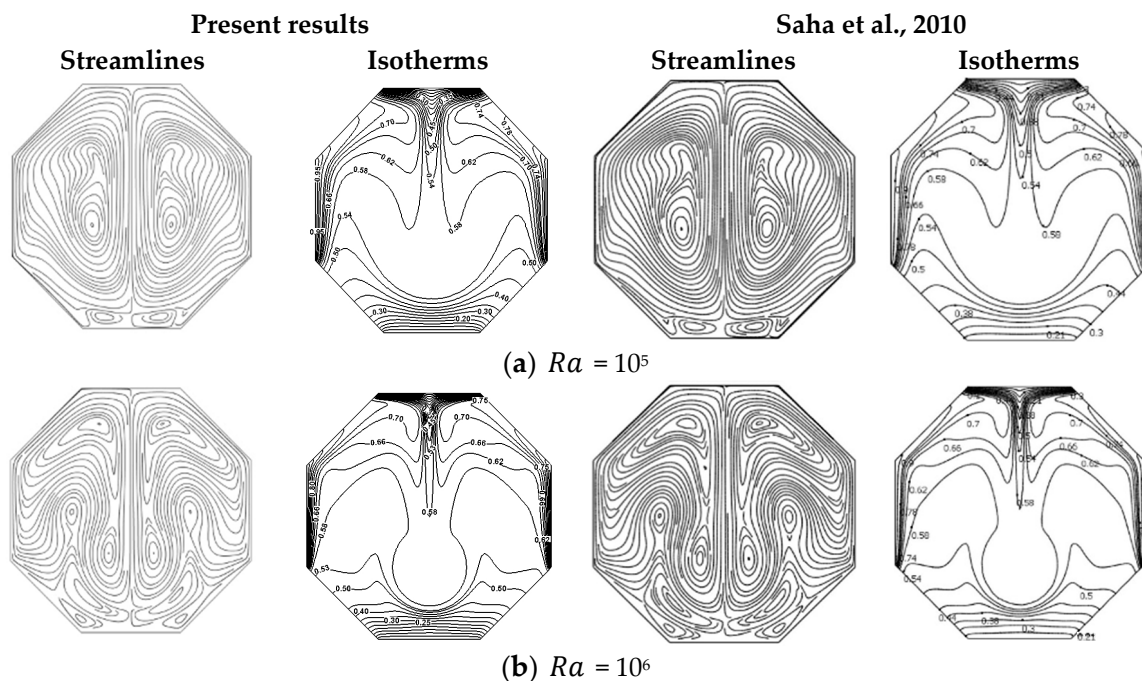
Streamline and isotherm profiles validation:

Figure 2. Comparison of the present streamlines and isotherms profiles with Saha et al. [35] for (**a**) $Ra = 10^5$ and (**b**) $Ra = 10^6$ with $Pr = 0.71$.

Isotherm profile validation:

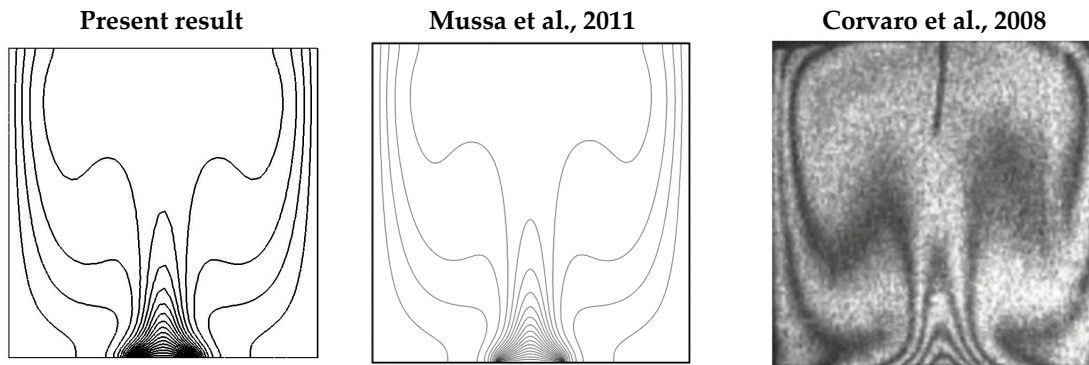| Present result | Mussa et al., 2011 | Corvaro et al., 2008 |

Figure 3. Comparison of the Isotherm between the present results, Mussa et al. [37] and the experimental results of Corvaro et al. [38] for $Ra = 2.02 \times 10^5$.
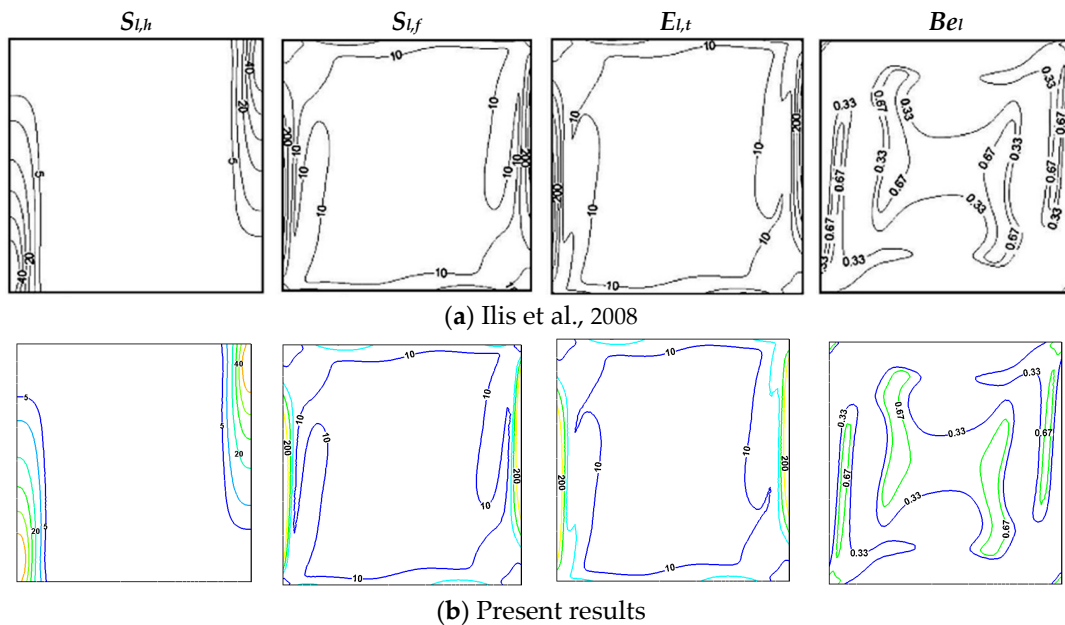
Entropy profiles validation:

Figure 4. Comparison of the $S_{l,h}$, $S_{l,f}$, $E_{l,t}$, and Be_l between the (**a**) Ilis et al. [36] and the (**b**) present results.

Table 2. Comparison of Nu_{avg} for various grid dimensions for $Ra = 10^6$, at $Pr = 0.71$ for air, $Pr = 7.00$ for water, and $Pr = 7.30$ for Al_2O_3-H_2O nanofluid.

	IBC		HFBC		
Elements	$Pr = 0.71$ (Air)	$Pr = 7.00$ (Water)	$Pr = 0.71$ (Air)	$Pr = 7.00$ (Water)	$Pr = 7.30$ ($\chi = 0.05$) Al_2O_3-H_2O Nanofluid
11,960	19.69	21.18	25.01	26.11	39.32
15,132	19.78	21.23	25.05	26.14	39.39
16,990	19.80	21.18	25.14	26.21	39.34
20,452	19.92	21.25	25.17	26.30	39.33
20,462	20.03	21.32	25.18	26.34	39.31
24,474	20.08	21.36	25.20	26.39	39.34
29,704	20.22	21.39	25.22	26.46	39.57
57,116	20.23	21.40	25.23	26.48	39.58

5. Use of Corcione [34] Empirical Correlation Model: A Justification

In 2011, Corcione [34] proposed a new empirical correlation model described in Equations (14)–(17) to determine the effective dynamic viscosity and thermal conductivity of nanofluids containing oxide and metal nanoparticles suspended in water or ethylene glycol-based solutions. The originality of this correlation is to demonstrate nanofluids' thermal conductivity depending on the nanoparticle concentration, temperature, and size. The model proposed for nanoparticles ranging in size from 10–150 nm and for nanoparticle concentrations ranging from 0.02–9%, with temperatures ranging from 294–324 K. It is worth mentioning that a phenomenon like dispersion/agglomeration of a certain degree caused by the suspended nanoparticles of different shapes and sizes happens to be observed in a discrete experimental setup. While deriving the empirical correlation, Corcione [34] did not consider this type of data set because of too sharp of a contrast in the data sets with an absence of enough physical evidence or observed spurious experimental results, or the presence of using chemical dispersants/surfactants during experiments, which causes agglomeration or significant changes in the thermo-mechanical behaviour of the suspension.

In 2013, Corcione et al. [39] expanded their work by investigating the HT behaviour within a square cavity using a two-phase mixture model with alumina-oxide nanofluids. In this work, they utilize the same empirical correlation model to estimate the thermal properties and successfully validate their empirical model with other experimental data for nanoparticle concentrations of 1–4%. Their research indicated that the increase in HT rate depended on the optimal particle loading, which was influenced by factors such as particle size, concentration, and micro-mixing convection resulting from the Brownian dynamics of the loaded nanoparticles.

In 2015, a study published by Cianfrini et al. [40] considered single-phase nanofluid modelling with temperature-dependent physical properties for nanoparticle loading up to 6%, in which nanofluids are treated as pure fluids such that the solid–liquid interface is in a thermal equilibrium state and the no-slip condition is preserved in the interface. Subsequently, Corcione et al. [41] conducted a similar study using two-phase modelling considering different boundary conditions and examined alumina-oxide, copper-oxide, and titanium dioxide nanofluids employing the same empirical correlation. They observed that the HT rate peaked at the optimal particle loading and subsequently decreased associated with the nanofluids' temperature and the difference between active walls.

Later, in 2018, Corcione et al. [41] also explored the two-phase modelling approach by investigating a slender vertical cavity filled with alumina-oxide nanofluids. They validated their findings for higher Ra ranges of 10^7 to 10^8 and concentrations up to 4%. Their results aligned with the earlier findings of Corcione et al. [39,41] in 2013 and 2015. The above discussion asserts that the Corcione proposed empirical correlation can be effectively utilized in nanofluid modelling both in single-phase and multi-phase approaches for volume fractions up to 6%. To validate the nanofluid simulation conducted in the present study, there is a comparison with the experimental study reported by Ho et al. [42] for nanoparticle volume fractions of 3% and 4%, as shown in Figure 5. The present numerical results closely resemble the experimental data, indicating that our model accurately captures the HT characteristics of the nanofluid. This agreement validates the reliability of our numerical approach and enhances our understanding of nanofluid HT phenomena.
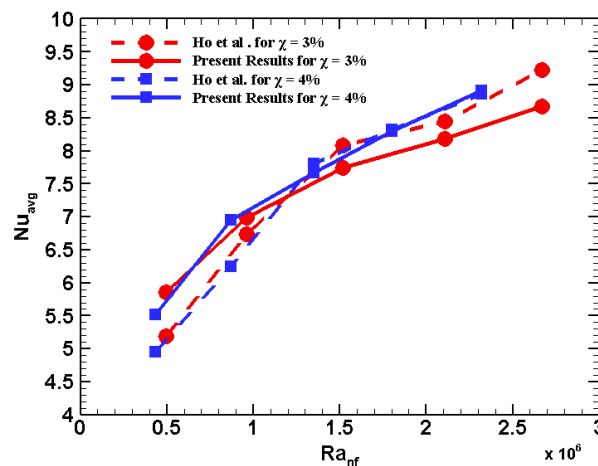
Figure 5. Comparison of the average Nu obtained from the present numerical simulation with the experimental results of Ho et al. [42] for $\chi = 3\%$ and $\chi = 4\%$.

6. Findings and Analysis

This numerical investigation examines the heat transfer and flow phenomena occurring within an enclosed space with an octagonal shape containing a cold cylinder. The study aims to explore the heat transfer characteristics of air, water, and Al_2O_3-H_2O nanofluid under different parameters, such as Ra ranging from 10^3 to 10^6, $Pr = 0.71$ for air and 7.0 for water, $Pr = 6.77$–7.30 for Al_2O_3-H_2O nanofluid, and χ varying between 1% to 5%. The nanofluid has a nanoparticles diameter (d_p) of 10 nm. This study will also analyze and compare the effects of IBC and HFBC on entropy generation. The subsequent sections will demonstrate the impact of the parameters mentioned above on the flow and temperature fields through the utilization of streamlines and isotherms. Furthermore, this study will investigate E_{gen} due to temperature gradient and viscous dissipation, as well as local E_{gen} and Be_l.

Table 3 displays the changes in Nu_{avg}, E_{avg}, and Be under isothermal boundary conditions, with and without a cylinder, for air and water. For air without a cylinder, the Nu_{avg} value increases from 2.42 to 11.22, the E_{avg} value increases from 2.62 to 1085.94, while the Be value decreases from 0.95 to 0.01, as the Ra value increases from 10^3 to 10^6. In contrast, for water without a cylinder, the Nu_{avg} value increases from 2.44 to 12.18, the E_{avg} value increases from 2.65 to 1370.57, while the Be value decreases from 0.94 to 0.01, as the Ra value increases from 10^3 to 10^6. Moreover, Table 3 shows that the Nu_{avg} and E_{avg} increase while Be decreases with an increase in Ra and the presence of a cylinder in the case of air. For all cases with $Ra = 10^3$ and 10^4, the Be values are greater than 0.5, indicating that E_{gen} due to temperature gradient is more significant than E_{gen} due to fluid friction. However, for $Ra = 10^5$ and 10^6, Be is less than 0.5, indicating that E_{gen} due to fluid friction is more dominant than E_{gen} due to temperature gradient. Furthermore, in the case of air subjected to a cylinder under the same isothermal boundary condition, the Nu_{avg} value rises from 3.43 to 20.22, the E_{avg} value increases from 3.73 to 1373.95, while the Be value drops from 0.94 to 0.015 with increasing Ra values from 10^3 to 10^6. For water subjected to a cylinder under the same isothermal boundary condition, the Nu_{avg} value rises from 3.44 to 21.39, the E_{avg} value increases from 3.74 to 1570.48, while the Be value drops from 0.94 to 0.01 with increasing Ra values from 10^3 to 10^6.

This suggests that the presence of the cylinder has a substantial effect on improving convective HT in air and water. The presence of the cold cylinder disrupts the flow patterns and creates flow recirculation zones. This leads to increased fluid mixing and enhanced HT through convective processes. In addition, the presence of the cylinder leads to an increase in Nu_{avg} and E_{avg} as the Ra value increases. As the Ra value increases from 10^3 to 10^6, the percentage increase in Nu_{avg} ranges from 41.88% to 80.16% in air and 40.95% to 75.58% in water, which further verifies the cylinder's capacity to improve convective HT and E_{gen}

in air and water. When comparing the results between air and water, we can observe that Nu_{avg} values are generally larger for water, indicating that convective HT is more efficient in water than in air. Nevertheless, the impact of the cylinder on Nu_{avg} is similar for both air and water, with a significant enhancement observed in both cases. According to Table 3, the cylinder's presence substantially improves convective HT in air and water. To better understand this impact, we will concentrate on the results acquired with the cylinder case rather than those without it.

Table 3. Variation of Nu_{avg}, E_{avg}, and Be using the isothermal boundary condition without cylinder and with cylinder for air and water.

	Without Cylinder			**With Cylinder**			
	Air						*Pr* = 0.71
Ra_f	Nu_{avg}	E_{avg}	Be	Nu_{avg}	E_{avg}	Be	**% Increase of Nu_{avg}**
10^3	2.42	2.62	0.95	3.43	3.73	0.94	41.88
10^4	4.20	7.38	0.58	6.70	11.18	0.61	59.70
10^5	6.81	58.75	0.12	11.42	88.32	0.13	67.61
10^6	11.22	1085.94	0.01	20.22	1373.95	0.015	80.16
	Water						*Pr* = 7.0
Ra_f	Nu_{avg}	E_{avg}	Be	Nu_{avg}	E_{avg}	Be	**% Increase of Nu_{avg}**
10^3	2.44	2.65	0.94	3.44	3.74	0.94	40.95
10^4	4.52	8.78	0.53	6.87	12.26	0.57	51.91
10^5	7.43	84.26	0.09	12.21	103.29	0.12	64.32
10^6	12.18	1370.57	0.01	21.39	1570.48	0.01	75.58

6.1. Variation of Streamline and Isotherm Profiles for Air/Water Case

Figure 6 displays the streamlines and isotherms of air and water for different Ra using IBC. In the case of $Ra = 10^3$, the streamline profiles present two identical rolls within the cavity of air and water. However, the isotherms are only symmetrical concerning the central vertical axis, while asymmetry is observed in the horizontal axis. This asymmetry is attributed to distinct convection effects encountered by the cavity's top and cold bottom walls and the cold cylinder. The temperature distribution inside the cavity is non-uniform and demonstrates significant variations across different regions. However, the temperature difference between neighboring regional points is small. It is worth noting that the isotherms located near the top cold wall and cylinder exhibit closely spaced contours, whereas those near the cold bottom wall possess flatter contours. Due to its higher density and thermal conductivity, water can transfer heat effectively more effectively than air. Therefore, at the same Ra, water generates larger and more stable convection cells than air, and its streamlines tend to be smoother and more regular than air flow patterns. As depicted in Figure 6, an increase in Ra significantly alters the isotherms and streamlines for both air and water cases. When Ra increases, the buoyancy forces that drive convection circulation become stronger, leading to a substantial deformation of the isotherms within the cavity. Specifically, at $Ra = 10^4$, there is an increase in the flow intensity, which is further amplified at $Ra = 10^5$ and $Ra = 10^6$. As for the air case, at $Ra = 10^5$, streamlines begin to form vertices, while in water, streamlines form two vertices near the cold bottom wall. Moreover, at $Ra = 10^6$, air streamlines form two vertices, and water streamlines form four vertices near the cold bottom wall. At higher Ra, streamlines exhibit more complexity and chaos than lower values, although they tend to be smoother and more regular than those observed in the air. With increasing Ra, convection circulation becomes stronger, causing the isotherms to become more tightly spaced near the two heat walls, the top cold wall,

and the cylinder, as is the case for $Ra = 10^5$ and $Ra = 10^6$. The isotherms become even more closely spaced than at lower values, denser than those observed in the air.
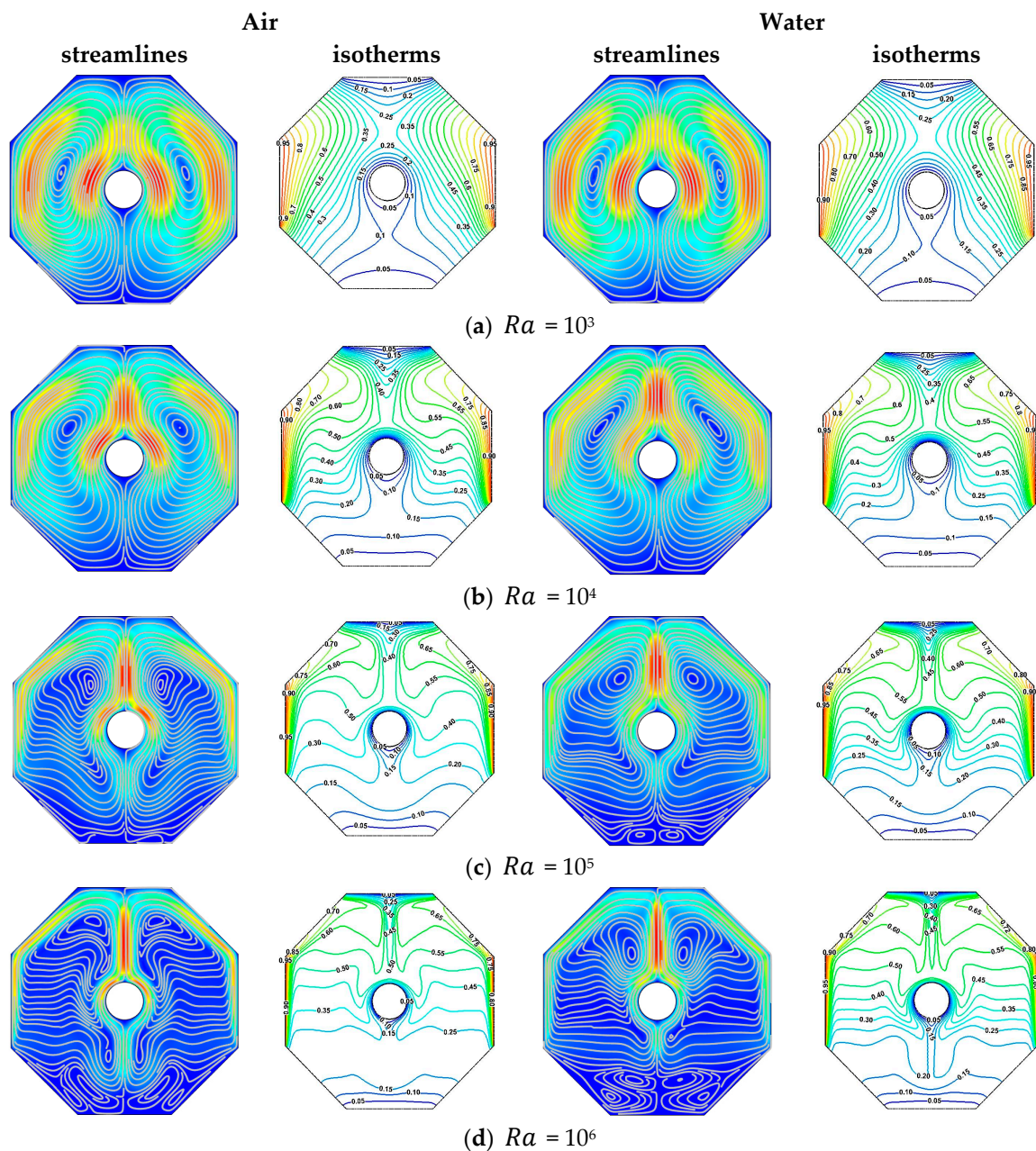
Air

Water

| streamlines | isotherms | streamlines | isotherms |

(**a**) $Ra = 10^3$

(**b**) $Ra = 10^4$

(**c**) $Ra = 10^5$

(**d**) $Ra = 10^6$

Figure 6. Distribution of streamlines and isotherms for (**a**) $Ra = 10^3$, (**b**) $Ra = 10^4$, (**c**) $Ra = 10^5$, and (**d**) $Ra = 10^6$ at $Pr = 0.71$ for air and $Pr = 7.0$ for water using IBC.

6.2. Variation of Different Entropy Production for Air/Water Cases

In Figure 7, E_{gen} due to temperature gradient and viscous dissipation, as well as the local E_{gen} and local Be for $Ra = 10^6$ for air and water using IBC, are shown. At this high Ra, the convective effects become dominant in determining the fluid flow and the amount of entropy generated, causing noticeable differences in E_{gen} between water and air. The higher heat conductivity and more significant convective effects of water result in higher magnitude changes in E_{gen} compared to air. The local E_{gen} and Be_l contours also display greater values in water than in air at $Ra = 10^6$, again attributed to the stronger convective effects in water leading to more significant inefficiency in fluid flow and greater entropy production.
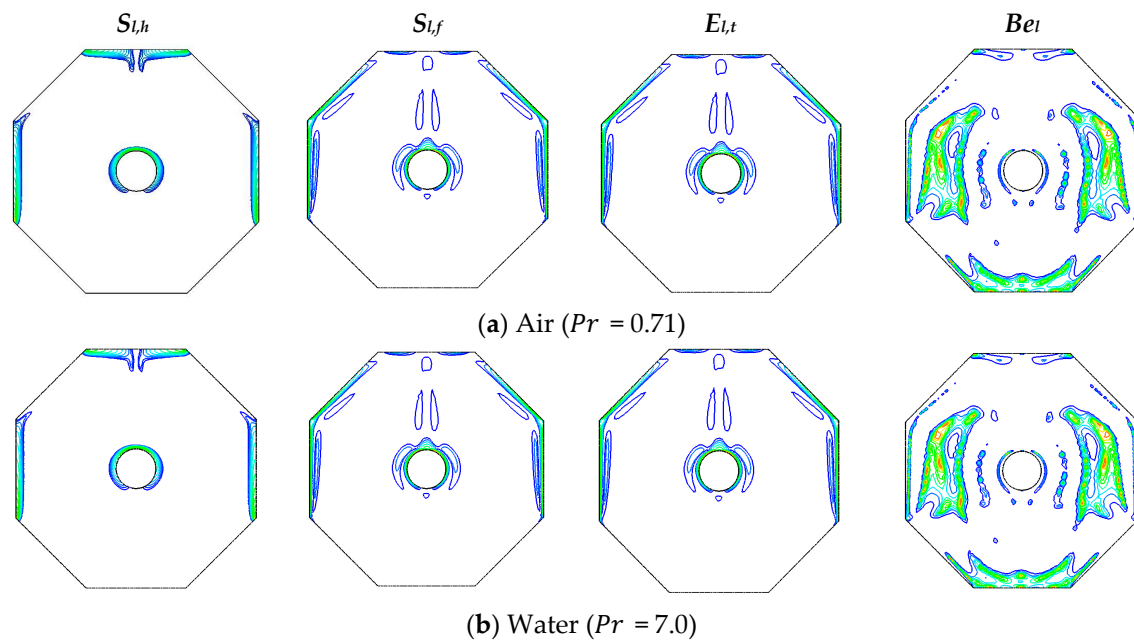
(**a**) Air (Pr = 0.71)

(**b**) Water (Pr = 7.0)

Figure 7. Distribution of local E_{gen} due to temperature gradient, viscous dissipation, local E_{gen}, and local B_{el} for (**a**) air and (**b**) water while $Ra = 10^6$ using IBC.

Table 4 shows that for both air and water under IBC and HFBC, Nu_{avg} increases and Be decreases as Ra increases. This is expected, as higher Ra values indicate greater temperature differences between the wall and fluid, resulting in increased heat transfer rates. Table 4 also shows that as the Ra value increases from 10^3 to 10^6, the average E_{gen} increases for air and water. The table also indicates that the average E_{gen} is lower when using HFBC than IBC for air and water. Furthermore, the average E_{gen} is higher for water than for air under both heating conditions. Table 4 demonstrates that the average E_{gen} is lower at lower values of Ra and higher at higher values of Ra. Regarding Be values, it can be observed that for both air and water at $Ra = 10^3$ under HFBC, Be is greater than 0.5. This implies that E_{gen}, due to temperature gradient, is more dominant than E_{gen} due to fluid friction. However, at Ra values of 10^4 to 10^6, Be values are less than 0.5, indicating that E_{gen} due to fluid friction is more dominant than E_{gen} due to the temperature gradient.

Table 4. Variation of Nu_{avg}, E_{avg}, and Be using IBC and HFBC for air and water.

	IBC			**HFBC**			
			Air				*Pr* = 0.71
Ra_f	Nu_{avg}	E_{avg}	Be	Nu_{avg}	E_{avg}	Be	% Increase of Nu_{avg}
10^3	3.43	3.73	0.94	5.90	0.37	0.92	72.11
10^4	6.70	11.25	0.61	9.78	0.84	0.25	45.97
10^5	11.42	88.32	0.13	16.00	6.18	0.021	40.13
10^6	20.22	1373.95	0.015	25.22	58.67	0.001	24.75
			Water				*Pr* = 7.0
Ra_f	Nu_{avg}	E_{avg}	Be	Nu_{avg}	E_{avg}	Be	% Increase of Nu_{avg}
10^3	3.44	3.74	0.94	5.91	0.37	0.92	71.75
10^4	6.87	12.26	0.57	9.92	0.85	0.25	44.32
10^5	12.21	103.29	0.12	16.63	6.81	0.018	36.26
10^6	21.39	1570.48	0.014	26.46	65.22	0.0012	23.70

Under IBC, in the case of air subjected to a cylinder, the Nu_{avg} value increases from 3.43 to 20.22, the E_{avg} value increases from 3.73 to 1373.95, while the *Be* value decreases from 0.94 to 0.015 with increasing *Ra* values from 10^3 to 10^6. Similarly, for water subjected to a cylinder, when the *Ra* value increases from 10^3 to 10^6, the Nu_{avg} value increases from 3.44 to 21.39, the E_{avg} value increases from 3.74 to 1570.48, and *Be* value decreases from 0.94 to 0.014. Under HFBC, in the case of air subjected to a cylinder, the Nu_{avg} value increases from 5.90 to 25.22, and the E_{avg} value increases from 0.37 to 58.67. In contrast, the *Be* value decreases from 0.92 to 0.001 values when *Ra* increases from 10^3 to 10^6. Similarly, for water subjected to a cylinder, when the *Ra* value increases from 10^3 to 10^6, the Nu_{avg} value increases from 5.91 to 26.46, the E_{avg} value increases from 0.37 to 65.22, and the *Be* value decreases from 0.92 to 0.0012.

Table 4 also reveals that the highest percent increase in Nu_{avg} for air and water occurs at the lowest *Ra* value of 10^3. This indicates that at lower *Ra* values, using HFBC has a more substantial effect on HT. When the *Ra* value increases, the percent increase in Nu_{avg} decreases for both air and water, indicating that the impact of HFBC is less pronounced at higher *Ra* values. HFBC involves maintaining a constant heat flux on the wall, causing the wall temperature to adjust accordingly. This generates a greater temperature difference between the wall and the fluid, resulting in a higher convective HT coefficient and, ultimately, a higher Nu_{avg}. By comparing the results for both air and water in Table 4, it is apparent that Nu_{avg} is generally greater for HFBC than for IBC. This suggests HT is more effective using HFBC.

Table 4 provides significant findings on the effect of boundary conditions on convective heat transfer and suggests that HFBC is more effective in enhancing convective heat transfer than IBC. For a better understanding of the effect of HFBC on convective heat transfer, we will focus on the results obtained with HFBC rather than the results obtained from IBC.

Figure 8 demonstrates that no vortices are formed near the bottom wall when the heat flux boundary condition is applied to air with $Ra = 10^6$. This is because HFBC controls the heat transfer rate at the walls, allowing for variation in temperature distribution. As a result, the heat transfer rate is more uniform near the bottom wall, leading to less temperature variation in the flow. This results in a smoother flow without any vortices near the bottom wall. Figure 8 shows that under HFBC, two vortices are formed near the bottom wall of the water. This is due to the higher thermal conductivity of water, which results in a greater heat transfer rate near the bottom wall. The streamlines and isotherms contours for air and water under HFBC indicate a more uniform heat distribution throughout the cavity. In addition, Figure 7 shows that using IBC leads to less efficient and uniform heat transfer throughout the cavity, while using HFBC (shown in Figure 8) results in higher local E_{gen} contours near the walls. This is because the smoother flow near the walls generates higher levels of viscous dissipation, which is a significant source of E_{gen}. Likewise, the local *Be* contours indicate higher values near the walls when implementing HFBC than IBC. When using HFBC, the elevated Be_l near the walls suggests more efficient HT in those areas.

We will explore the potential benefits of using nanofluids in natural convection to enhance HT and reduce E_{gen}. We will investigate the impact of different concentrations of nanoparticles on system performance, as well as the influence of a cold cylinder on the natural convection system, which is highly effective in improving HT and reducing E_{gen}. Moreover, we will examine how the application of HFBC can further enhance HT and reduce E_{gen} in natural convection. Finally, we will assess the system's environmental impact by evaluating its Ecological Coefficient Performance (ECOP). All of these details will be presented in the following analysis.
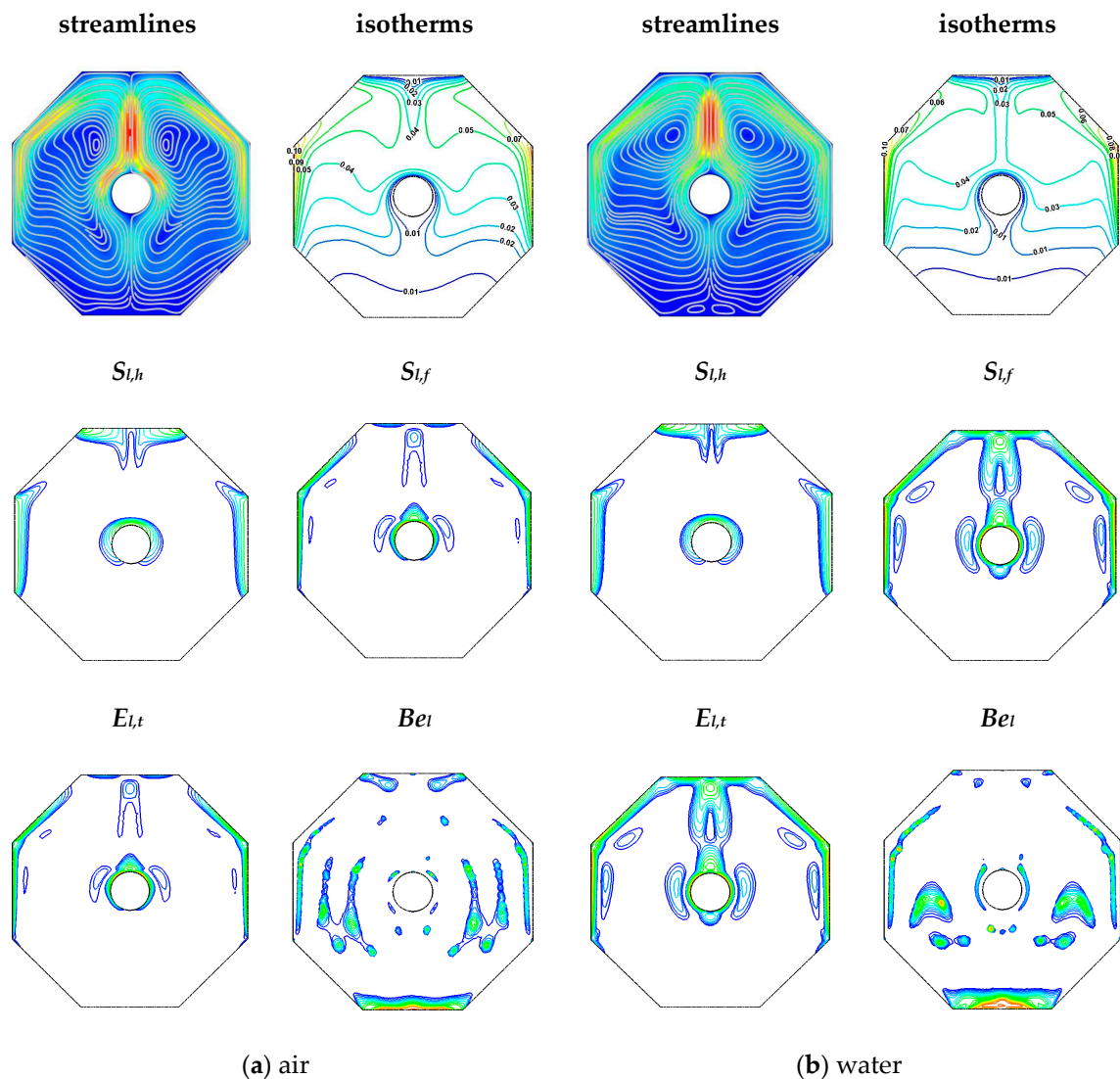
Figure 8. Distribution of streamlines, isotherms, E_{gen} due to temperature gradient, viscous dissipation, local E_{gen}, and local Be while $Ra = 10^6$ using HFBC for (**a**) air and (**b**) water.

6.3. Variation of Streamline, Isotherm, Local E_{gen}, and Be for Al_2O_3-H_2O Nanofluid Subject to Different Ra

Figure 9 plots the streamlines, isotherms, $E_{l,t}$, and Be_l for various Ra while maintaining a constant χ of 5%. The streamline profiles indicate the presence of two core vortices inside the cavity. As Ra increases, the buoyancy force increases, causing the core vortices to rise. This leads to a faster rate of convective HT, resulting in a more efficient HT process within the cavity. The isotherm contours reveal that as Ra increases, the contours become denser in proximity to the heated and cold walls and in the vicinity of the cold cylinder. This suggests that the denser contours near the non-insulated walls play a crucial role in influencing the HT efficiency of the cavity. In addition to the streamline and isotherm contours, Figure 9 demonstrates that altering Ra impacts the local entropy and Be_l contours for χ of 5%. Examining the local entropy contours, we observe that as Ra increases, the graphs become denser in the vicinity of the heated and cold cylinders while decreasing in the lower half. Moreover, the local entropy contours show that the graphs become denser in the upper half of the cavity, resulting in an increase in entropy in that region. As for local Be, for the lower Ra values ($Ra = 10^3$ and $Ra = 10^4$), the graphs are uniformly distributed throughout the cavity, indicating a uniform HT distribution. However, as Ra increases, the

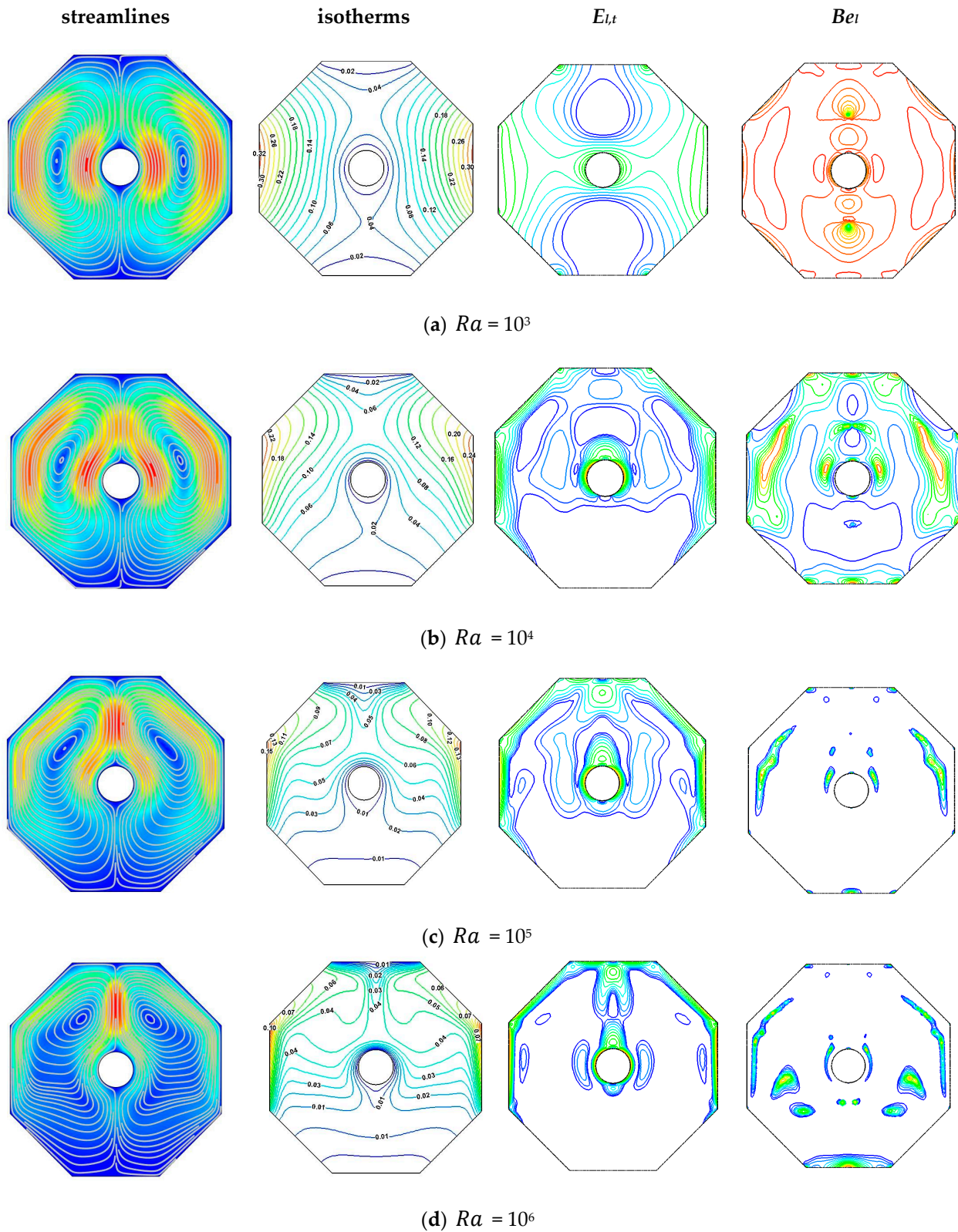graphs become denser near the lower cold wall, suggesting a decrease in the rate of HT in that particular region.

streamlines	**isotherms**	$E_{l,t}$	Be_l

(**a**) $Ra = 10^3$

(**b**) $Ra = 10^4$

(**c**) $Ra = 10^5$

(**d**) $Ra = 10^6$

Figure 9. Variation of streamlines, isotherms, local E_{gen}, and Be_l for (**a**) $Ra = 10^3$, (**b**) $Ra = 10^4$, (**c**) $Ra = 10^5$, and (**d**) $Ra = 10^6$ at $\chi = 5\%$.

6.4. Variation of Entropy for Different χ

The behavior of E_{gen} due to the temperature gradient, viscous dissipation, local E_{gen}, and local Be contours can vary significantly when using nanofluids, depending on χ as shown in Figure 10. Including nanoparticles in the fluid increases its thermal conductivity, resulting in a reduced temperature gradient and E_{gen} caused by the temperature gradient. As χ in the nanofluid increases from 1% to 5%, the effective thermal conductivity of the fluid also increases, leading to further reductions in temperature gradient and E_{gen} due to the temperature gradient. Figure 10 exhibits that at a constant $Ra = 10^6$, increasing χ has a minimal impact on E_{gen} due to temperature. However, as χ increases from 1% to 5%, the entropy generated due to viscous dissipation and local E_{gen} decreases. Additionally, Be_l for nanofluids increases with increasing χ, indicating a less effective HT process. The rise in Be_l with an increase in χ suggests a decrease in the efficiency of HT in the cavity.
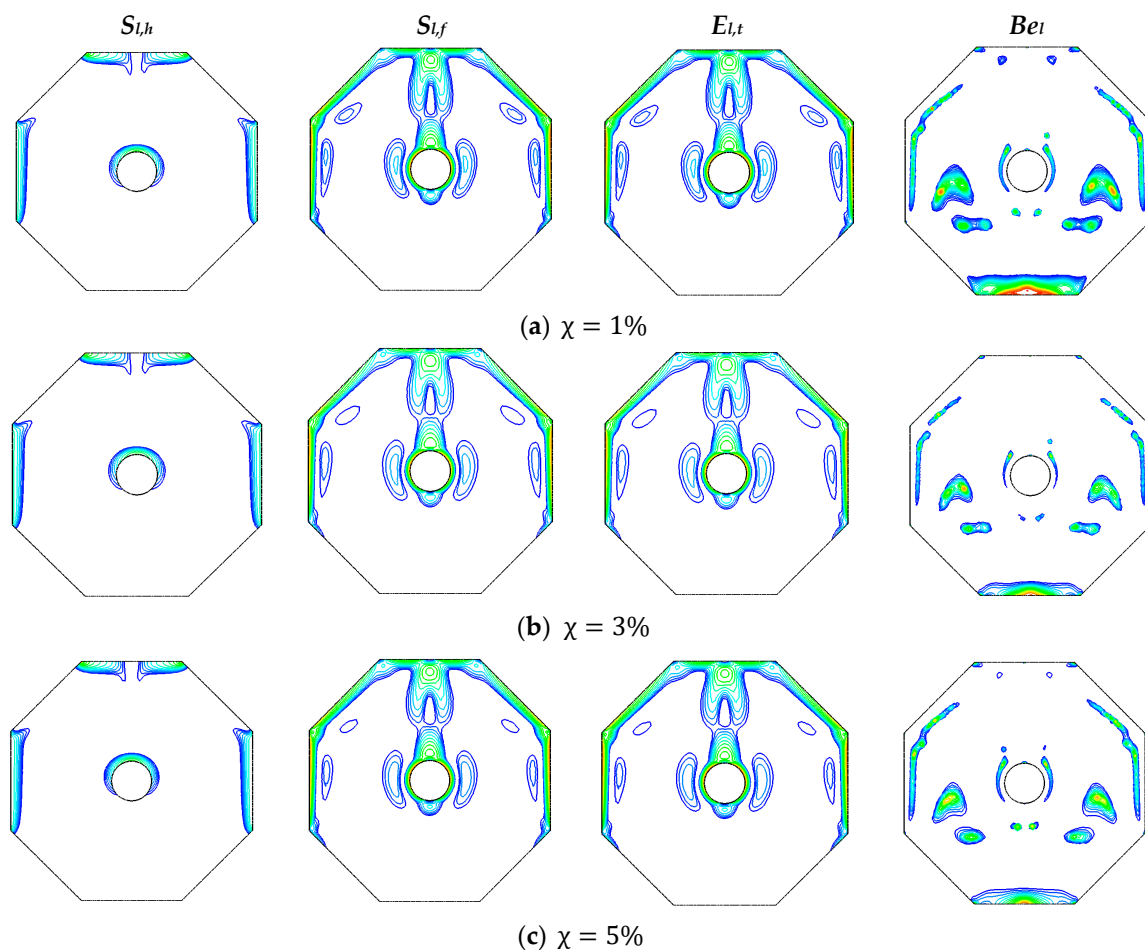

Figure 10. Distribution of E_{gen} due to temperature gradient, viscous dissipation, local E_{gen}, and local Be for (**a**) $\chi = 1\%$, (**b**) $\chi = 3\%$, and (**c**) $\chi = 5\%$, at $Ra = 10^6$.

Table 5 displays the relationship between Nu_{avg} and varying χ under different Ra for HFBC. Additionally, the percentage of Nu_{avg} enhancement (E% $= \frac{Nu_{avg}\ (\chi \neq 0) - Nu_{avg}\ (\chi = 0)}{Nu_{avg}\ (\chi = 0)} \times 100$) in comparison to the base fluid is provided for each scenario. When Ra is 10^3, increasing χ from 1% to 5% results in a substantial increase in both Nu_{avg} and enhancement percentage. Specifically, Nu_{avg} increases from 6.34 to 7.77, and the enhancement percentage increases from 7.38% to 31.57%. Similarly, for Ra of 10^4, Nu_{avg} increases from 10.64 to 11.29, and the enhancement percentage increases from 7.25% to 13.78%. The pattern observed in Table 5 is consistent for Ra values of 10^5 and 10^6. Specifically, for $Ra = 10^5$, Nu_{avg} increases from 18.08 to 19.86, and the enhancement percentage increases from 8.69% to 19.42% when χ increases

from 1% to 5%. For $Ra = 10^6$, Nu_{avg} increases from 28.69 to 31.89, and the enhancement percentage increases from 8.45% to 20.56% with the same increase in χ. This increase in χ results in a corresponding increase in thermal conductivity and convective HT, ultimately leading to higher Nu_{avg} values. Additionally, Table 5 illustrates that the enhancement percentage in Nu_{avg} increases with increasing χ, indicating that adding nanoparticles to the base fluid enhances the rate of HT.

Table 5. Variation of Nu_{avg} and heat transfer enhancement (E%) with different χ for HFBC.

	$Ra = 10^3$		$Ra = 10^4$		$Ra = 10^5$		$Ra = 10^6$	
	Nu_{avg}	E (%)	Nu_{avg}	E (%)	Nu_{avg}	E (%)	Nu_{avg}	E (%)
$\chi = 1\%$	6.34	7.38	10.64	7.25	18.08	8.69	28.69	8.45
$\chi = 2\%$	6.85	16.01	11.03	11.17	18.79	13.00	29.80	12.64
$\chi = 3\%$	7.20	21.85	11.13	12.18	19.22	15.54	30.57	15.54
$\chi = 4\%$	7.37	24.72	11.25	13.40	19.64	18.11	31.29	18.28
$\chi = 5\%$	7.77	31.57	11.29	13.78	19.86	19.42	31.89	20.56

As the nanoparticle's χ increases, the overall thermal conductivity of the nanofluid also increases. This enhancement in thermal conductivity facilitates more efficient HT within the cavity, leading to higher HT rates. This also increases Brownian motion, which aids in dispersing heat more uniformly throughout the cavity, thereby enhancing HT.

Table 6 presents the relationship between Be and varying χ and Ra under HFBC. When Ra is 10^3, increasing χ from 1% to 5% increases Be from 0.93 to 0.98. Similarly, for $Ra = 10^4$, Be increases from 0.25 to 0.35. The trend continues for Ra values of 10^5 and 10^6, where Be increases with increasing χ. For $Ra = 10^5$, Be increases slightly from 0.017 to 0.019, whereas for $Ra = 10^6$, Be appears to remain constant, increasing from 0.0011 to 0.0013. This indicates that when Ra is held constant, increasing χ results in higher Be values, signifying a greater rate of convective HT than the rate of E_{gen}. Table 6 further reveals that for $Ra = 10^3$, all χ (1–5%) yield Be values greater than 0.5, indicating that E_{gen} due to temperature gradient is more significant than E_{gen} due to fluid friction. However, for $Ra = 10^4$, $Ra = 10^5$, and $Ra = 10^6$, all χ result in Be values less than 0.5, suggesting that E_{gen} due to fluid friction is more dominant than E_{gen} due to temperature gradient.

Table 6. Variation of Be with different χ for HFBC.

	$Ra = 10^3$	$Ra = 10^4$	$Ra = 10^5$	$Ra = 10^6$
$\chi = 1\%$	0.93396	0.24515	0.01722	0.00114
$\chi = 2\%$	0.94602	0.25493	0.01724	0.00114
$\chi = 3\%$	0.95657	0.27131	0.01738	0.00115
$\chi = 4\%$	0.96666	0.29741	0.01778	0.00116
$\chi = 5\%$	0.97569	0.35121	0.01890	0.00131

Table 7 depicts the variation of average entropy with varying χ for HFBC at different Ra. The E_{avg} decreases for all Ra as χ increases from 1% to 5%. For instance, at $Ra = 10^3$, the E_{avg} decreases from 0.38 to 0.32 as χ increases from 1% to 5%. Similarly, for $Ra = 10^4$, the E_{avg} decreases from 0.84 to 0.79, for $Ra = 10^5$, the E_{avg} decreases from 6.68 to 6.32, and for $Ra = 10^6$, the E_{avg} decreases from 64.75 to 61.72. This indicates that increasing χ decreases the cavity's overall entropy. The reason behind this reduction in entropy is attributed to the enhanced thermal conductivity and convective heat transfer due to the presence of nanoparticles. These properties facilitate more efficient heat transfer within the cavity, leading to a reduction in entropy. Therefore, adding nanoparticles can improve the system's thermal performance but at the expense of a decrease in the overall entropy.

Table 7. Variation of average entropy with different χ for HFBC.

	$Ra = 10^3$	$Ra = 10^4$	$Ra = 10^5$	$Ra = 10^6$
$\chi = 1\%$	0.3811	0.8437	6.6832	64.7459
$\chi = 2\%$	0.3503	0.8274	6.6609	64.3995
$\chi = 3\%$	0.3370	0.8236	6.5913	64.1616
$\chi = 4\%$	0.3308	0.8073	6.4776	63.1396
$\chi = 5\%$	0.3208	0.7976	6.3161	61.7198

Table 8 depicts how the Ecological Coefficient Performance $\left(ECOP = \frac{Nu_{avg}}{E_{avg}} \right)$ is affected by varying Ra, given a heat flux boundary condition. Results show that, at $Ra = 10^3$, increasing from 1% to 5% causes ECOP to increase from 16.64 to 24.22. Similarly, at $Ra = 10^4$, ECOP rises from 12.78 to 14.21. The pattern of ECOP values for $Ra = 10^5$ and 10^6 is also similar, with an increase in ECOP from 2.70 to 3.03 at $Ra = 10^5$, and from 0.44 to 0.52 at $Ra = 10^6$. In general, an increase from 1% to 5% leads to a higher ECOP, indicating that adding nanoparticles to the fluid enhances energy efficiency and reduces environmental impact. By increasing ECOP through volume concentration, nanoparticles can improve energy and environmental efficiency. Additionally, Table 8 reveals that as Ra increases from 10^3 to 10^6, there is a decrease in ECOP values, implying reduced energy efficiency and a higher environmental impact. This trend suggests that higher Ra values may result in lower ECOP values, potentially indicating a reduction in energy efficiency and an increase in the system's environmental impact.

Table 8. Ecological Coefficient Performance (ECOP) with different χ for HFBC.

	$Ra = 10^3$	$Ra = 10^4$	$Ra = 10^5$	$Ra = 10^6$
$\chi = 1\%$	16.6405	12.7796	2.6997	0.4431
$\chi = 2\%$	19.5577	13.6847	2.8410	0.4627
$\chi = 3\%$	21.3561	13.6978	2.8787	0.4764
$\chi = 4\%$	21.6150	14.0579	3.0077	0.4956
$\chi = 5\%$	24.2235	14.2051	3.0283	0.5168

6.5. Proposed Correlation for Nu_{avg}

In this section, a formula is introduced that establishes a correlation between Nu_{avg} and three factors: Ra, Pr, and χ. The construction of the correlation model for Nu_{avg} is based on the values for $10^3 \leq Ra \leq 10^6$, $1\% \leq \chi \leq 5\%$, $Pr = 6.77$ to 7.30. Based on the mentioned assumptions, we propose the following general form for the correlation:

$$Nu_{avg} = f + a\left(Ra^b + Pr^c + 100\,\chi\,d \right) \tag{26}$$

where $a = 1.918599$, $b = 0.199469$, $c = 0.179773$, $d = 0.29138858$, and $f = -4.78256978$.

Furthermore, the accuracy of the predicted data acquired from the proposed model in relation to the actual data for Nu_{avg} is visually depicted in Figure 11. The correlation between the predicted and actual data, as indicated by an R^2 value of 0.99, demonstrates a strong agreement. Notably, the comparison between the actual values and Equation (26) reveals a satisfactory level of concordance. Critically, the analysis of residual plots confirms that the non-linear multiple regression model proposed in Equation (26) exhibits a bias concerning the actual values.
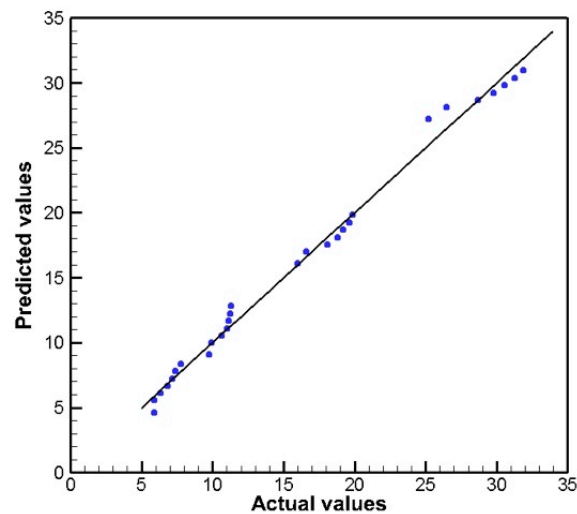
Figure 11. Comparison between actual values and predicted values for Nu_{avg}.

7. Conclusions

The current investigation analyzed ways to improve HT and E_{gen} in an octagonal cavity with a cylinder by varying χ, Pr, Ra, and the boundary conditions (IBC and HFBC). The presence of the cold cylinder within the cavity has been found to have a significant impact on the system's heat transfer characteristics, resulting in enhanced heat transfer performance. This observation emphasizes the importance of considering the geometrical arrangement of the cavity and its influence on heat transfer processes. Implementation of HFBC for both air and water leads to higher Nu_{avg} and lower E_{avg} in comparison to IBC. This highlights the effectiveness of HFBC in improving heat transfer and reducing entropy generation, thereby enhancing the overall thermal performance of the system. The study's key findings are the following:

- The presence of a cold cylinder within the cavity significantly impacts the system's heat transfer characteristics, increasing heat transfer;
- Using HFBC for air and water results in a higher Nu_{avg} and lower E_{avg} than IBC;
- At lower Ra ($Ra = 10^3$), Nu_{avg} increases the most for air and water when HFBC is applied;
- The addition of nanoparticles enhances HT, and as χ increases, the rate of HT also increases;
- The average E_{gen} rises with an increase in Ra, and at higher values of Ra, such as $Ra = 10^6$, the average E_{gen} is higher;
- Increasing χ in a fluid leads to improved energy efficiency and reduced environmental impact;
- The rise in Ra from 10^3 to 10^6 results in a reduction in energy efficiency and an increased environmental impact.

In the present study, the observation of particle clustering and its impact on the effective viscosity of the nanofluids has not been considered. This phenomenon may have a substantial impact on the convective heat transfer phenomenon. Our study serves as a preliminary investigation, providing insights into natural convection behavior under simplified conditions. Further studies considering the clustering effect would be necessary for a more comprehensive understanding of nanofluid behavior in realistic scenarios. The future perspective of the present study can be considered to be the following:

- The study is focused on the natural convection flow and heat transfer phenomenon and does not account for forced convection;
- Ra is limited to the range of 10^3 to 10^6 for laminar flow in this study, but higher values of Ra could be considered in future research;

- The investigation is limited to specific parameters for fluid flow and heat transfer characteristics. Other factors, such as cylinder shape, size, and cavity orientation, could impact the system's behavior and should be studied in future research;
- The study only considers the Al_2O_3-H_2O nanofluid, and other types of nanofluids with different properties and characteristics may exhibit different behavior under similar conditions;
- In future research, the possibility of investigating the effects of moving the fixed cold cylinder towards the walls of the cavity could provide valuable insights into the system's thermal behavior;
- Future research can explore the clustering effects and mass transport of particles to gain a deeper understanding of their impact on the system.

Nomenclature

C_p	Specific heat capacity (J/kg K)
D	Einstein diffusion coefficient (J/K)
d_f	Fluid molecular diameter (nm)
d_p	Diameter of nanoparticle (nm)
E_{gen}	Entropy generation
L	Length (m)
M	Molecular weight of the base fluid (kg/mole)
N	Avogadro number
Nu_{avg}	Average Nusselt number
p	Pressure (N/m^2)
Pr	Prandtl number
Be	Bejan number
Ra	Rayleigh number
Re	Reynolds number
k	Thermal conductivity (W/m K)
U	Dimensionless horizontal velocity component
V	Dimensionless vertical velocity component
X	Dimensionless horizontal coordinate
Y	Dimensionless vertical coordinate
P	Dimensionless pressure
q''	Heat flux (W/m^2)
$\hat{n}$	Outward normal vector
T_0	Reference temperature (K)
r	Radius of the cylinder (m)

T	Temperature (K)
T_{fr}	Freezing point of the base fluid (K)
T_h	High temperature (K)
T_c	Cold temperature (K)
u_B	Nanoparticle mean Brownian velocity (m/s)
k_b	Boltzmann constant (J/K)
v	Velocity (m/s)
x, y	Cartesian coordinates (m)
g	Gravitational acceleration (ms^{-2})
$S_{l,h}$	Entropy generation due to temperature gradient
$S_{l,f}$	Entropy generation due to viscous dissipation
$E_{l,t}$	Local entropy generation
E_{avg}	Average entropy generation
Be_l	Local Bejan number
Greek symbols	
ρ	Density (kg/m^3)
π	pi
α	Thermal diffusivity (m^2/s)
ν	Kinematic viscosity (m^2/s)
μ	Dynamic viscosity (kg/m s)
β	Thermal expansion coefficient (K^{-1})
Θ	Non-dimensional temperature
λ	Irreversibility factor
χ	Nanoparticles volume concentration
τ_D	Time (s)
Subscripts	
f	Base fluid
nf	Nanofluid
p	Particle
avg	Average

References

1. Alsabery, A.I.; Ishak, M.S.; Chamkha, A.J.; Hashim, I. Entropy generation analysis and natural convection in a nanofluid-filled square cavity with a concentric solid insert and different temperature distributions. *Entropy* **2018**, *20*, 336. [CrossRef]
2. Ismail, F.; Hasan, M.N.; Saha, S.C. Numerical study of turbulent fluid flow and heat transfer in lateral perforated extended surfaces. *Energy* **2014**, *64*, 632–639. [CrossRef]
3. Sheremet, M.A.; Oztop, H.F.; Pop, I.; Abu-Hamdeh, N. Analysis of entropy generation in natural convection of nanofluid inside a square cavity having hot solid block: Tiwari and Das' Model. *Entropy* **2015**, *18*, 9. [CrossRef]
4. Selimefendigil, F.; Öztop, H.F. Natural convection and entropy generation of nanofluid filled cavity having different shaped obstacles under the influence of magnetic field and internal heat generation. *J. Taiwan Inst. Chem. Eng.* **2015**, *56*, 42–56. [CrossRef]
5. Selimefendigil, F.; Öztop, H.F. MHD mixed convection and entropy generation of power law fluids in a cavity with a partial heater under the effect of a rotating cylinder. *Int. J. Heat Mass Transf.* **2016**, *98*, 40–51. [CrossRef]
6. Siavashi, M.; Bordbar, V.; Rahnama, P. Heat transfer and entropy generation study of non-Darcy double-diffusive natural convection in inclined porous enclosures with different source configurations. *Appl. Therm. Eng.* **2017**, *110*, 1462–1475. [CrossRef]
7. Wang, T.; Huang, Z.; Xi, G. Entropy generation for mixed convection in a square cavity containing a rotating circular cylinder using a local radial basis function method. *Int. J. Heat Mass Transf.* **2017**, *106*, 1063–1073. [CrossRef]
8. Rahimi, A.; Kasaeipoor, A.; Malekshah, E.H.; Kolsi, L. Natural convection analysis by entropy generation and heatline visualization using lattice Boltzmann method in nanofluid filled cavity included with internal heaters- Empirical thermo-physical properties. *Int. J. Mech. Sci.* **2017**, *133*, 199–216. [CrossRef]
9. Rahimi, A.; Kasaeipoor, A.; Malekshah, E.H.; Palizian, M.; Kolsi, L. Lattice Boltzmann numerical method for natural convection and entropy generation in cavity with refrigerant rigid body filled with DWCNTs-water nanofluid-experimental thermo-physical properties. *Therm. Sci. Eng. Prog.* **2018**, *5*, 372–387. [CrossRef]
10. Kefayati, G.; Tang, H. MHD thermosolutal natural convection and entropy generation of Carreau fluid in a heated enclosure with two inner circular cold cylinders, using LBM. *Int. J. Heat Mass Transf.* **2018**, *126*, 508–530. [CrossRef]
11. Arun, S.; Satheesh, A. Mesoscopic analysis of MHD double diffusive natural convection and entropy generation in an enclosure filled with liquid metal. *J. Taiwan Inst. Chem. Eng.* **2019**, *95*, 155–173. [CrossRef]
12. Bozorg, M.V.; Siavashi, M. Two-phase mixed convection heat transfer and entropy generation analysis of a non-Newtonian nanofluid inside a cavity with internal rotating heater and cooler. *Int. J. Mech. Sci.* **2019**, *151*, 842–857. [CrossRef]

13. Alsabery, A.I.; Gedik, E.; Chamkha, A.J.; Hashim, I. Impacts of heated rotating inner cylinder and two-phase nanofluid model on entropy generation and mixed convection in a square cavity. *Heat Mass Transf.* **2019**, *56*, 321–338. [CrossRef]
14. Alsabery, A.; Selimefendigil, F.; Hashim, I.; Chamkha, A.; Ghalambaz, M. Fluid-structure interaction analysis of entropy generation and mixed convection inside a cavity with flexible right wall and heated rotating cylinder. *Int. J. Heat Mass Transf.* **2019**, *140*, 331–345. [CrossRef]
15. Ahrar, A.J.; Djavareshkian, M.H.; Ahrar, A. Numerical simulation of Al$_2$O$_3$-water nanofluid heat transfer and entropy generation in a cavity using a novel TVD hybrid LB method under the influence of an external magnetic field source. *Therm. Sci. Eng. Prog.* **2019**, *14*, 100416. [CrossRef]
16. Tayebi, T.; Chamkha, A.J. Entropy generation analysis due to MHD natural convection flow in a cavity occupied with hybrid nanofluid and equipped with a conducting hollow cylinder. *J. Therm. Anal. Calorim.* **2019**, *139*, 2165–2179. [CrossRef]
17. Tasmin, M.; Nag, P.; Hoque, Z.T.; Molla, M. Non-Newtonian effect on heat transfer and entropy generation of natural convection nanofluid flow inside a vertical wavy porous cavity. *SN Appl. Sci.* **2021**, *3*, 299. [CrossRef]
18. Li, Z.; Hussein, A.K.; Younis, O.; Afrand, M.; Feng, S. Natural convection and entropy generation of a nanofluid around a circular baffle inside an inclined square cavity under thermal radiation and magnetic field effects. *Int. Commun. Heat Mass Transf.* **2020**, *116*, 104650. [CrossRef]
19. Kashyap, D.; Dass, A.K.; Oztop, H.F.; Abu-Hamdeh, N. Multiple-relaxation-time lattice Boltzmann analysis of entropy generation in a hot-block-inserted square cavity for different Prandtl numbers. *Int. J. Therm. Sci.* **2021**, *165*, 106948. [CrossRef]
20. Hamzah, H.; Canpolat, C.; Jasim, L.M.; Sahin, B. Hydrothermal index and entropy generation of a heated cylinder placed between two oppositely rotating cylinders in a vented cavity. *Int. J. Mech. Sci.* **2021**, *201*, 106465. [CrossRef]
21. Ahlawat, A.; Sharma, M.K. Effects of heated block comprised porous stratum and micropolar hybrid nanofluid on convective heat transfer and entropy generation in a square enclosure. *Heat Transf.* **2022**, *51*, 5320–5347. [CrossRef]
22. Majeed, A.H.; Mahmood, R.; Shahzad, H.; Pasha, A.A.; Islam, N.; Rahman, M.M. Numerical simulation of thermal flows and entropy generation of magnetized hybrid nanomaterials filled in a hexagonal cavity. *Case Stud. Therm. Eng.* **2022**, *39*, 102293. [CrossRef]
23. Acharya, N. On the hydrothermal behavior and entropy analysis of buoyancy-driven magnetohydrodynamic hybrid nanofluid flow within an octagonal enclosure fitted with fins: Application to thermal energy storage. *J. Energy Storage* **2022**, *53*, 105198. [CrossRef]
24. Ikram, M.M.; Saha, G.; Saha, S.C. Conjugate forced convection transient flow and heat transfer analysis in a hexagonal, partitioned, air-filled cavity with dynamic modulator. *Int. J. Heat Mass Transf.* **2021**, *167*, 120786. [CrossRef]
25. Ikram, M.M.; Saha, G.; Saha, S.C. Unsteady conjugate heat transfer characteristics in hexagonal cavity equipped with a multi-blade dynamic modulator. *Int. J. Heat Mass Transf.* **2023**, *200*, 123527. [CrossRef]
26. Saha, G.; Al-Waaly, A.A.; Paul, M.C.; Saha, S.C. Heat transfer in cavities: Configurative systematic review. *Energies* **2023**, *16*, 2338. [CrossRef]
27. Sharma, B.K.; Kumar, A.; Gandhi, R.; Bhatti, M.M.; Mishra, N.K. Entropy generation and thermal radiation analysis of EMHD Jeffrey nanofluid flow: Applications in solar energy. *Nanomaterials* **2023**, *13*, 544. [CrossRef]
28. Almuhtady, A.; Alhazmi, M.; Al-Kouz, W.; Raizah, Z.A.S.; Ahmed, S.E. Entropy generation and MHD convection within an inclined trapezoidal heated by triangular fin and filled by a variable porous media. *Appl. Sci.* **2021**, *11*, 1951. [CrossRef]
29. Ahmed, S.E.; Rashed, Z.Z. MHD natural convection in a heat generating porous medium-filled wavy enclosures using Buongiorno's nanofluid model. *Case Stud. Therm. Eng.* **2019**, *1*, 100430. [CrossRef]
30. Ahmed, S.E.; Raizah, Z.A. FEM treatments for MHD radiative convective flow of MWCNTs C$_2$H$_6$O$_2$ nanofluids between inclined hexagonal/hexagonal or hexagonal/cylinder. *Ain Shams Eng. J.* **2022**, *13*, 101549. [CrossRef]
31. Raizah, Z.A.S.; Alsabery, A.I.; Aly, A.M.; Hashim, I. Energy and entropy production of nanofluid within an annulus partly saturated by a porous region. *Entropy* **2021**, *23*, 1237. [CrossRef] [PubMed]
32. Masuda, H.; Ebata, A.; Teramae, K.; Hishinuma, N. Alteration of thermal conductivity and viscosity of liquid by dispersing ultra-fine particles. Dispersion of Al$_2$O$_3$, SiO$_2$ and TiO$_2$ Ultra-Fine Particles. *Netsu Bussei* **1993**, *7*, 227–233. [CrossRef]
33. Nag, P.; Molla, M. Double-diffusive natural convection of non-Newtonian nanofluid considering thermal dispersion of nanoparticles in a vertical wavy enclosure. *AIP Adv.* **2021**, *11*, 095219. [CrossRef]
34. Corcione, M. Empirical correlating equations for predicting the effective thermal conductivity and dynamic viscosity of nanofluids. *Energy Convers. Manag.* **2011**, *52*, 789–793. [CrossRef]
35. Saha, G.; Saha, S.; Hasan, M.N.; Islam, M.Q. Natural convection heat transfer within octagonal cavity. *Int. J. Eng. Trans. A Basics* **2010**, *23*, 1–10.
36. Ilis, G.G.; Mobedi, M.; Sunden, B. Effect of aspect ratio on entropy generation in a rectangular cavity with differentially heated vertical walls. *Int. Commun. Heat Mass Transf.* **2008**, *35*, 696–703. [CrossRef]
37. Mussa, M.; Abdullah, S.; Azwadi, C.N.; Muhamad, N. Simulation of natural convection heat transfer in an enclosure by the lattice-Boltzmann method. *Comput. Fluids* **2011**, *44*, 162–168. [CrossRef]
38. Corvaro, F.; Paroncini, M. A numerical and experimental analysis on the natural convective heat transfer of a small heating strip located on the floor of a square cavity. *Appl. Therm. Eng.* **2008**, *28*, 25–35. [CrossRef]
39. Corcione, M.; Cianfrini, M.; Quintino, A. Two-phase mixture modeling of natural convection of nanofluids with temperature-dependent properties. *Int. J. Therm. Sci.* **2013**, *71*, 182–195. [CrossRef]

40. Cianfrini, M.; Corcione, M.; Quintino, A. Natural convection in square enclosures differentially heated at sides using alumina-water nanofluids with temperature-dependent physical properties. *Therm. Sci.* **2015**, *19*, 591–608. [CrossRef]

41. Corcione, M.; Grignaffini, S.; Quintino, A.; Ricci, E.; Vallati, A. Buoyancy-Induced Convection of Alumina-Water Nanofluids in Laterally Heated Vertical Slender Cavities. *Heat Transf. Eng.* **2018**, *39*, 1103–1116. [CrossRef]

42. Ho, C.; Liu, W.; Chang, Y.; Lin, C. Natural convection heat transfer of alumina-water nanofluid in vertical square enclosures: An experimental study. *Int. J. Therm. Sci.* **2010**, *49*, 1345–1353. [CrossRef]